

1
2 **Exploring the Temporal-Varying and Depth-Nonlinear Velocity Profile of Debris**
3 **Flows Based on A Stratification Statistical Algorithm for 3D-HBP-SPH Particles**

4
5
6
7 **Zheng HAN^{1,2}, Wendou XIE¹, Chuicheng ZENG¹, Yange LI^{1,3*}, Changli LI¹, Haohui**
8 **DING¹, Weidong WANG¹, Ningsheng CHEN⁴, Guisheng HU⁴, Guangqi CHEN⁵**

9
10
11 ¹ School of Civil Engineering, Central South University, Changsha 410075, China.

12 ² Hunan Provincial Key Laboratory for Disaster Prevention and Mitigation of Rail Transit
13 Engineering Structures, Changsha 410075, China.

14 ³ The Key Laboratory of Engineering Structures of Heavy Haul Railway, Ministry of Education,
15 Changsha 410075, China.

16 ⁴ Key Lab of Mountain Hazards and Surface Processes, Institute of Mountain Hazards and
17 Environment, Chinese Academy of Sciences, Chengdu 610041, China.

18 ⁵ Department of Civil Engineering, Kyushu University, Fukuoka, 819-0395, Japan.

19
20
21 Corresponding author: Y. Li (liyange@csu.edu.cn), No.22 Shaoshan South Road, School of Civil
22 Engineering, Central South University, Changsha, Hunan, China. Tel.: +86 18684982076.

23
24
25
26 **Key Points:**

- 27
- A stratification statistical algorithm for interpreting the dynamics of 3D-HBP-SPH particles is introduced.
 - A logarithmic-based model for the temporal-varying and depth-nonlinear velocity profile is regressed.
 - 34 sets of velocity data measured in different flume experiments are used to verify the proposed model.
- 28
29
30
31
32
33

34 Abstract

35 Estimation of velocity profile through mud depth is a long-standing and essential problem in
36 debris-flow dynamics. Until now, various velocity profiles have been proposed based on the
37 regression of experimental measurements, but these are often limited by the observation
38 conditions, such as the number of the configured sensors. Therefore, the resulting linear velocity
39 profiles exhibit limitations in reproducing the nonlinear behavior and its temporal variation
40 during the debris-flow process. In this study, we present a novel approach to explore debris-flow
41 velocity profile in detail upon our previous 3D-HBP-SPH numerical model, i.e., the three-
42 dimensional Smoothed Particle Hydrodynamic model incorporating with the Herschel-Bulkley-
43 Papanastasiou rheology. Specifically, we propose a stratification statistical algorithm for
44 interpreting the details of SPH particles, which enables the recording of temporal velocities of
45 debris flow at different mud depths. To regress the velocity profile, we introduce a logarithmic-
46 based nonlinear function with two empirical parameters, that a controlling the shape of velocity
47 profile and b concerning its temporal evolution. We verify the proposed velocity profile and
48 explore its sensitivity using 34 sets of velocity data from three individual flume experiments in
49 previous literatures. Our results demonstrate that the proposed temporal-varying and depth-
50 nonlinear velocity profile outperforms the previous ones.

51 Plain Language Summary

52 Studies of debris-flow dynamics involves estimating the velocity profile through mud depth.
53 Conventional velocity profiles in previous studies were limited by observation conditions and
54 were unable to reproduce the nonlinear behaviour and its temporal variation. Here, we propose a
55 new approach to explore debris-flow velocity profiles through three-dimensional numerical
56 simulation using the smoothed particle hydrodynamic (SPH) method. A stratification statistical
57 algorithm is introduced to analyse the details of SPH particles based on the numerical results to
58 record and output temporal velocities of debris flow at different mud depths. A logarithmic-
59 based function with two parameters is introduced to regress the nonlinear velocity profile with
60 temporal variation. It is verified using 34 sets of velocity data from three individual flume
61 experiments. The results show that the proposed depth-nonlinear and temporal-varying velocity
62 profile performs better than previous ones.

63 1 Introduction

64 Debris flows are highly sediment-laden flows mixing with mud, stones, organic materials, and
65 water, travelling at high velocities in steep channels. This kind of fluid–solid flows pose severe
66 risks to residential societies at the mountainous area, and often cause serious casualties and
67 property losses worldwide each year (Dowling & Santi, 2014; Godt & Coe, 2007; VanDine &
68 Bovis, 2002). Their unpredictable initiation, tremendous destructive power, and long run-out
69 distance represent a challenging task of engineering design and plan for hazard mitigation and
70 prevention. Many catastrophic cases have been reported recent years, for example, the August 8,
71 2010, Zhouqu debris flow event destroying approximately 5500 buildings in China (Chen et al.,
72 2019; Tang et al., 2011), as well as the 2003 debris flow events at the Faucon region damaging
73 many existed sabo dams in the Swiss Alps (Remaître et al., 2008).

74 The tremendous destructive power of debris flows can be explained in part by their high
75 travelling velocities. Therefore, predicting on the debris-flow velocity has long been an essential
76 issue on the topic of debris-flow mitigation research. In fact, as a typical two-phase phenomenon,

77 debris-flow velocity distribution is one of the most complex problems in the dynamic mechanism
 78 due to the flow's opacity caused by its high concentration of solid particles (Rickenmann, 1999;
 79 Han et al., 2015a; Chen et al., 2017). Moreover, inertial collision of the solid particles, coarse
 80 grain friction, viscous shear, and interaction between solid and fluid phase during the debris-flow
 81 process arise uncertainties and difficulties when estimating its travelling velocities (Du et al.,
 82 2021; Iverson, 1997). Therefore, it remains a great scientific challenge to provide an exact
 83 solution for describing the complex flowing behavior of debris flows.

84 In this sense, a common and acceptable solution is to reduce its complexity by representing the
 85 debris-flow velocity field into the lateral distribution and the vertical profile through a cross-
 86 section. As to the lateral distribution, common wisdom often holds that debris-flow velocity is
 87 greater along the thalweg and getting smaller at both sides of the channel (Han et al., 2015a).
 88 Many remarkable studies can be referred to, such as the experimental investigation by Iverson et
 89 al. (2001) and Tecca et al. (2003), as well as the theoretical solution in our previous study (Han
 90 et al., 2014). Also, many numerical models based on the depth-averaged Navier-Stokes equations
 91 (e.g., Luna et al. 2012; Ouyang et al., 2015) have been employed to investigate the velocity of
 92 debris flow.

93 Nevertheless, the vertical velocity profile of the debris flow shows more complicated dynamics
 94 due to the high concentration and frequent collisions of solid particles. The velocity profile of
 95 debris flow relates to its internal deformation, holding essential information on hydrodynamics
 96 and flow resistance. Generally, the overall features of the debris-flow velocity profile have been
 97 discussed and substantiated in many previous studies, that the velocity at the free surface is much
 98 higher than that at the fluid bottom (Johnson et al., 2012). Nagl et al. (2020) summarized four
 99 possible types of velocity profile, i.e., constant velocity profile with full basal sliding, flow
 100 profile over rigid bed with no basal sliding, combination of basal sliding and internal
 101 deformation, and flow over an erodible bed. They mentioned that the vertical velocity profiles
 102 are strongly linked to flow characteristics such as pore-fluid pressure, grain size distribution and
 103 density variations.

104 Systematic measurements of velocity profiles in real-scale debris flows are not yet available
 105 (Nagl et al., 2020), therefore, flume experiments are an alternative way to investigate the
 106 complex phenomenon of debris-flow velocity profile (Wei & Hu, 2009). Many previous studies
 107 used measurement devices, such as ultrasonic sensors, radar, or seismic sensors, to obtain the
 108 debris flow velocities (e.g., Arattano & Marchi, 2005; Chen et al., 2017; Iverson & Vallance,
 109 2001; Johnson et al., 2012; Nagl et al., 2020; Prochaska et al., 2008; Tecca et al., 2003; Wei et
 110 al., 2012). These previous studies well documented the measurement data of vertical velocities
 111 and provided an insight into the velocity profile of debris flow. Based on the observed features of
 112 vertical velocity distribution, some linear or non-linear velocity profile have been assumed, such
 113 as in Hotta and Ohta (2000), Johnson et al. (2012), and Han et al. (2015a). Notably, these
 114 established velocity profiles in different studies commonly have a similar form which can be
 115 expressed as below,

$$v(z) = f\left(\alpha, \left(\frac{z}{h}\right)^\beta\right) \quad (1)$$

116 where f denotes the velocity profile, z is the vertical location beyond the bed, h is the flow
 117 depth. α presents an empirical parameter controlling the amount of shear within the bulk of flow.
 118 β denotes an another parameter controlling linear or nonlinear behavior considering basal slip.
 119 However, owing to that in most of the flume experiments, the amount of the velocimeter sensors

120 in the array is limited, difficulties arise when regressing a good-fitting nonlinear profile with
121 such limited amount of measurement data. Also, the best-fitting values of the involved empirical
122 parameters α and β are currently debated among the existing studies. In view of this, the single-
123 parameter linear velocity profiles, and have been applied in many numerical studies (e.g.,
124 Ouyang et al., 2015; Han et al., 2015b).

125 Intense velocity data through the depth definitely benefits a better regression of debris-flow
126 velocity profile. Recently, particle image velocimetry (PIV) has been witnessed a great potential
127 in exploring the dynamics of two-phase flows due to its non-invasive measurement, full-field,
128 instantaneous flow velocity maps (Gabriele et al., 2011; Liu & Lam, 2015). Owing to that direct
129 measurements for opaque debris flows are problematic (Iverson, 2012), therefore, for better
130 observation of tracer particles, high fluid transparency and relatively low solid concentration
131 should be considered. Many studies, e.g., Chen et al. (2017) used mixture of machine oil and
132 white oil to represent the debris flow fluid with a similar viscosity. Regardless of the argument
133 that whether oil-mixture is adequate for representing debris-flow fluid, the PIV-based
134 experimental data demonstrates a more obvious nonlinear velocity profile. Many previous
135 studies, e.g., Chen et al. (2017), Du et al., (2021) and Han et al. (2022), recommended a usage of
136 logarithm-based function to regress the nonlinear velocity profile, which could better fit with the
137 experimental measurements.

138 However, it should be noticed that velocity profile of debris flows has not yet been well
139 recognized. One key problem is with respect to the temporal variation of the debris-flow velocity
140 profile. In most of the previous experimental studies, capturing the instantaneous velocity at
141 different depths is a tough task. This difficulty commonly lies in the measurement using either
142 the image-based velocimetry of PIV or the ultrasonic sensor-based velocimetry in flume
143 experiments. Meanwhile, uncertainties due to collision of the solid particles bring noises in the
144 measurement data, which are difficult to recognize and denoise. Therefore, mean velocity at
145 different depths during the debris flow process has to be used, which inherently hides the feature
146 of temporal variation.

147 Besides, the debris-flow event may occur as a single surge or as a sequence of multiple surges
148 (e.g., Arai et al., 2013; Zanuttigh & Lamberti, 2007). Even in a surge, the inhomogeneous debris-
149 flow mass has been observed complex dynamics, that turbulence flow at the debris flow surge
150 front would transit into a laminar one at the surge end when debris flow passes by Pudasaini et
151 al. (2020). As a consequence, the velocity profile varies with the flow status. Evidence could be
152 found in the remarkable real-scale experiment by Nagl et al. (2020), that velocity profiles at the
153 front part, the main body show obvious different shapes. This concept and evidence inspired the
154 subsequent research on how the observed temporal variation could be considered in the
155 regression of debris-flow velocity profile.

156 In this paper, based on the proposed 3D-HBP-SPH numerical model (Han et al., 2021a), we
157 reproduce the debris-flow flume experiments by Iverson et al. (2011) where debris-flow
158 dynamics were well-documented. We propose a particle-location based stratification statistical
159 algorithm to analyze the temporal velocities at different depth. With the interpreted temporal
160 velocity distribution, a double-parameter, logarithmic-based function is regressed to describe the
161 velocity profile variation with time-elapse. The measurements of velocity data presented in other
162 three previous flume experiment by Egashira et al. (1989), Hotta et al. (1998) and Chen et al.
163 (2017) are used to illustrate the effect of the proposed temporal-varying and depth-nonlinear
164 velocity profile.

165 2 Methodologies

166 2.1 The proposed 3D-HBP-SPH numerical model

167 As mentioned above, a better regression of debris-flow velocity profile depends on a greater
 168 amount of velocity data at different depth. Many flume experimental studies used ultrasonic
 169 sensors to measure debris-flow velocities. However, due to the size of the sensors, the total
 170 number of the sensors are limited, the collected measurement data are insufficient to present the
 171 observed nonlinear velocity profile in other PIV-based experiments.

172 Therefore, in this paper, we use particle-based numerical model to explore the debris-flow
 173 velocity profile. In general, this kind of particle-based model provides a 3D description of the
 174 debris-flow dynamic process through discrete particles and approximately solves the Navier-
 175 Stokes (N-S) equations in discrete form (Hung & McDougall, 2009; McDougall & Hung,
 176 2005), so that a large amount of debris-flow dynamic data can be recorded. Considering the
 177 complex rheology of debris-flow mass, here we use our previous three-dimensional SPH model
 178 based on Herschel-Bulkley-Papanastasiou (HBP) rheology (Han et al., 2019, 2021a), the so-
 179 called 3D-HBP-SPH model, the positive effect of which has been substantiated by the following
 180 studies (Huang et al., 2022; Morikawa & Asai, 2022; Yu et al., 2020). The details of the model
 181 could be referred to Han et al. (2019) and Han et al. (2021a), while the basics of this model is
 182 introduced in detail in the supporting information Text S1 along with this paper. With the
 183 termination of the numerical simulation using 3D-HBP-SPH model, the debris-flow process is
 184 able to be reproduced because the spatial positions (x, y, z) and velocity components (v_x, v_y, v_z)
 185 of SPH particles at different time steps are well-documented and sorted.

186 2.2 Particle stratification statistical algorithm

187 It should be noted that a total of approximately 10^5 to 10^6 SPH particles are commonly used to
 188 represent debris-flow mass in a three-dimensional simulation, each of these particles shows
 189 different spatial positions and velocity vectors. It is inadequate to simply choose some among all
 190 the particles for regressing the velocity profile, because the chosen particles could not be able to
 191 describe the overall behavior of debris flow. In this sense, all the particles must be
 192 comprehensively considered.

193 These recorded dynamic data in particle form should be processed before they can be further
 194 used to demonstrate the debris-flow velocity profile. In this paper, a major contribution is with
 195 respect to the particle stratification statistical algorithm, which is specifically designed to analyze
 196 the temporal average velocity of the SPH particles at different flow depths. The proposed
 197 algorithm is introduced as following.

198 2.2.1 Coordinate system transformation

199 The numerical simulation result of the 3D-HBP-SPH model is a time-series dataset, with a time
 200 interval Δt . In a certain time step t , the spatial positions (x, y, z) and velocity components
 201 (v_x, v_y, v_z) of each particle along X, Y, Z directions are included. However, the physical
 202 variables of the particles in the SPH scheme are described in absolute coordinates. To better
 203 understand the velocity profile, the velocity component (v_x, v_y, v_z) of each particle in absolute
 204 coordinates should be transformed into the flume bed-linked local coordinate system (X', Y', Z')

205 (as shown in [Figure 1b](#)), so that the velocities along the bed can be conventionally represented by
 206 v_X . The method for coordinate system transformation is expressed by

$$\begin{bmatrix} x' \\ y' \\ z' \end{bmatrix} = R(\theta_X)R(\theta_Y)R(\theta_Z) \begin{bmatrix} x \\ y \\ z \end{bmatrix} - \begin{bmatrix} x_{origin} \\ y_{origin} \\ z_{origin} \end{bmatrix} \quad (2a)$$

$$\begin{bmatrix} v'_X \\ v'_Y \\ v'_Z \end{bmatrix} = R(\theta_X)R(\theta_Y)R(\theta_Z) \begin{bmatrix} v_X \\ v_Y \\ v_Z \end{bmatrix} \quad (2b)$$

207 where x_{origin} , y_{origin} , and z_{origin} denotes the origin of the absolute coordinate in the numerical
 208 result. $R(\theta_X)$, $R(\theta_Y)$, $R(\theta_Z)$ are the rotation matrixes depending on the inclined angles of the bed
 209 along the X , Y , and Z directions, respectively.

$$R(\theta_X) = \begin{bmatrix} \cos(\theta_X) & 0 & -\sin(\theta_X) \\ 0 & 1 & 0 \\ \sin(\theta_X) & 0 & \cos(\theta_X) \end{bmatrix} \quad (3a)$$

$$R(\theta_Y) = \begin{bmatrix} 1 & 0 & 0 \\ 0 & \cos(\theta_Y) & \sin(\theta_Y) \\ 0 & -\sin(\theta_Y) & \cos(\theta_Y) \end{bmatrix} \quad (3b)$$

$$R(\theta_Z) = \begin{bmatrix} 1 & 0 & 0 \\ 0 & 1 & 0 \\ 0 & 0 & 1 \end{bmatrix} \quad (3c)$$

210 where θ_X and θ_Y are the inclined angles of the bed along X and Y directions. Normally, for the
 211 single-section flume, we assume the flume along the X direction. In this case, θ_Y equates 0 and

$$212 \quad R(\theta_Y) = \begin{bmatrix} 1 & 0 & 0 \\ 0 & 1 & 0 \\ 0 & 0 & 1 \end{bmatrix}.$$

213 **2.2.2 Particle recognition in the domain of the cross-section**

214 Velocity profile represents vertical velocity distribution of a selected cross-section. In the
 215 numerical simulation results of 3D-HBP-SPH, once a cross-section at $x' = x'_0$ is selected, the
 216 particles those passing through this cross-section should be recognized and filtered. However,
 217 even though a large number of particles are used in the numerical simulation, the particles those
 218 coincidentally passing through the cross-section may be rare. To get a sufficient velocity data for
 219 regressing the velocity profile, here as shown in [Figure 1c](#), we expand the selected cross-section
 220 backward and forward for a small distance which we named as the domain length L_{domain} . Thus,
 221 the particles with the instantaneous spatial position (x', y', z') that satisfying the criterion
 222 $x' \in [x'_0 - L_{domain}, x'_0 + L_{domain}]$ are supposed within the domain of the selected cross-section,
 223 and should be considered in the regression of the velocity profile in this cross-section.

224 2.2.3 Particles stratification according to their position

225 Suppose that there are totally n particles in the cross-section domain, with various vertical
 226 position z'_i along the Z' direction. The maximum vertical position is $z'_{max} = \max(z'_1, z'_2, \dots, z'_n)$
 227 and the minimum one is $z'_{min} = \min(z'_1, z'_2, \dots, z'_n)$. Assume a small height Δh pseudo layer, the
 228 cross-section domain could be stratified into m layers, that

$$m = \frac{z'_{max} - z'_{min}}{\Delta h} \quad (4)$$

229 and the vertical location of each layer is

$$H_j = z'_{min} + \Delta h(j - 1), (j = 1, 2, \dots, m). \quad (5)$$

230 Thus, the particles with the vertical position z' that satisfying the criterion $z' \in [H_j, H_{j+1}]$ are
 231 supposed belonging to the layer j , and a total number k_j of the particle in each layer j can be
 232 counted.

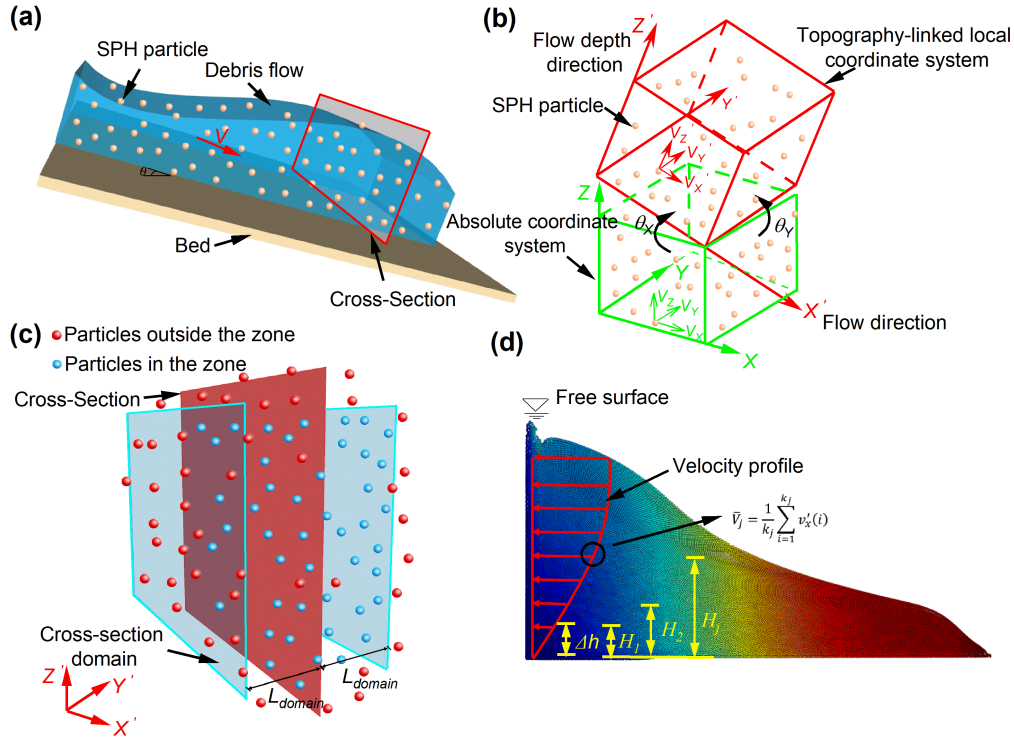
233 2.2.4 Velocity evaluation of each stratified layer

234 The above-mentioned algorithm has recognized k_j particles belonging to the layer j . Each
 235 particle has velocity components (v'_x, v'_y, v'_z) which have been transformed from (v_x, v_y, v_z) in
 236 the absolute coordinate. Among three velocity components, v'_y denotes the velocity across the
 237 section, v'_z is the particle velocity through flow depth, while v'_x describes the velocity along the
 238 flume. Therefore, as illustrated in [Figure 1d](#), we use the mean value of the velocity component
 239 v'_x of each recognized particle to determine the representative velocity of the layer j , which is
 240 expressed as

$$\bar{V}_j = \frac{1}{k_j} \sum_{i=1}^{k_j} v'_x(i). \quad (6)$$

241 where \bar{V}_j is the output velocity of debris flow at the vertical position of $z = H_j$.

242 The schematic illustration of the proposed particle stratification statistical algorithm is illustrated
 243 in [Figure 1](#). In this way, a series of mean velocities $(\bar{V}_1, \bar{V}_2, \dots, \bar{V}_j)$ at different vertical positions
 244 can be obtained and further used for the regression of the velocity profile.



245

246 **Figure 1.** Schematic illustration of the particle hierarchical statistical algorithm. (a) Illustration
 247 of the particle-based debris flow process. (b) Coordinate system transformation. (c) Particle
 248 recognition in the domain of the cross-section. (d) Particles stratification and velocity evaluation
 249 of each stratified layer.

250 3 Numerical reproduction of the flume experiment

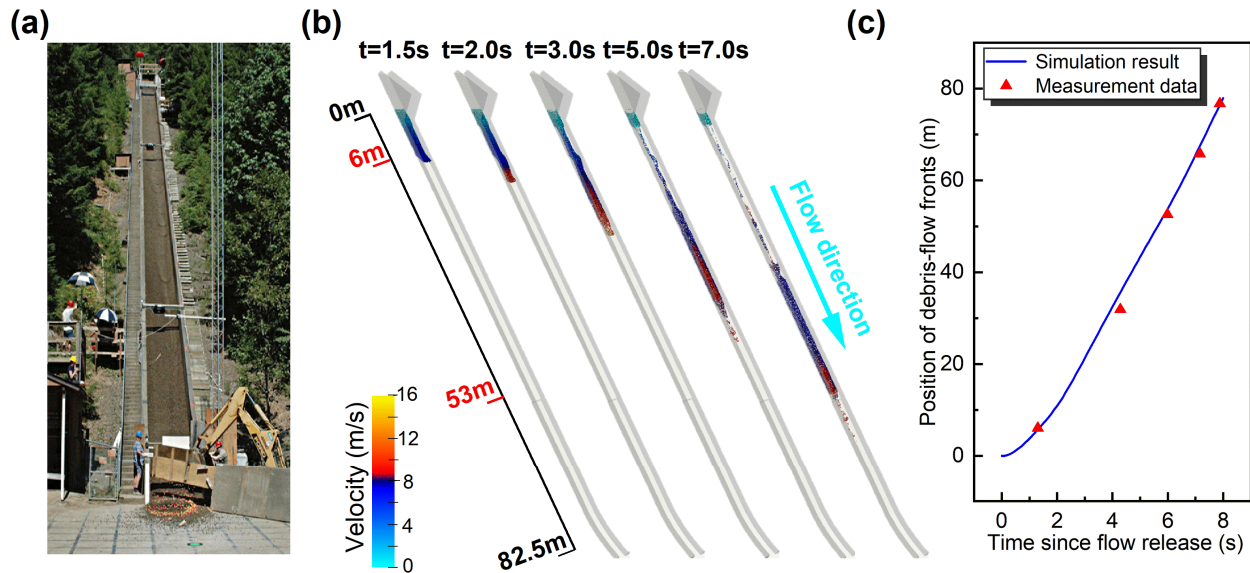
251 3.1 Numerical simulation of USGS flume test

252 As we have mentioned above, systematic measurements of velocity profiles in real-scale debris
 253 flows are not yet available (Nagl et al., 2020). Therefore, flume experiments with well-
 254 documented measurement data become an alternative way, in particular that the flattened flume
 255 avoids the influence of complex topography to the debris-flow dynamics in real-scale event. In
 256 this paper, we select the USGS flume experiment reported in detail in Iverson et al. (2011) for
 257 numerical reproduction. The large-scale flume experiment was designed to explore the positive
 258 feedback and momentum growth during debris flow entrainment process and achieved
 259 remarkable findings those inspired the following studies. The large-scale flume has a straight
 260 concrete channel that 95m in length and 2m in width, inclined at an angle of 31°. As arrays of
 261 electronic sensors had been installed in the flume, the dynamics of the experimental debris-flow
 262 process, e.g., temporal variation of flow depth, were well-documented and recorded, which could
 263 be essential to calibrate the numerical simulation for reproducing this experiment.

264 This flume experiment has been simulated in our previous study (Han et al., 2022), where a total
 265 of 43,258 fluid particles were used to represent the discretized debris-flow mass in the
 266 experiment. Nevertheless, in order to better explore the velocity details, more fluid particles are
 267 necessary to minimize the uncertainties of particle distribution. In this study, a total of 87,951
 268 fluid particles are generated to discretize the debris-flow mass, which is almost two times more

269 than our previous studies. While 486,694 fixed boundary particles are used to represent the flume
 270 structure. As we choose a very small time increment $\Delta t = 0.0001s$ in the numerical simulation,
 271 the computational consumption might be high. Therefore, a high-performance computational
 272 server, capable of 24 core Intel Xeon Scalable CPU, 2 pieces of NVIDIA Titan V GPU, and
 273 128GB RAM, is employed to execute the numerical computing. Other configurations and values
 274 of key parameters are kept the same as we summarized and listed in the previous study (Han et
 275 al., 2022).

276 The debris-flow process that 25s in duration takes almost 48 hours to complete the numerical
 277 reproduction. With two-times more particles adopted, the simulation results in Figure 2b show
 278 more details for the subsequent exploring of debris flow velocities. To verify the simulation
 279 results, the observed positions of debris-flow front in the experiment at different times are used
 280 as benchmarks and are compared with the numerical results (as shown in Figure 2c). It is
 281 demonstrated that the simulation results are in a good accordance with the observation in the
 282 experiment.



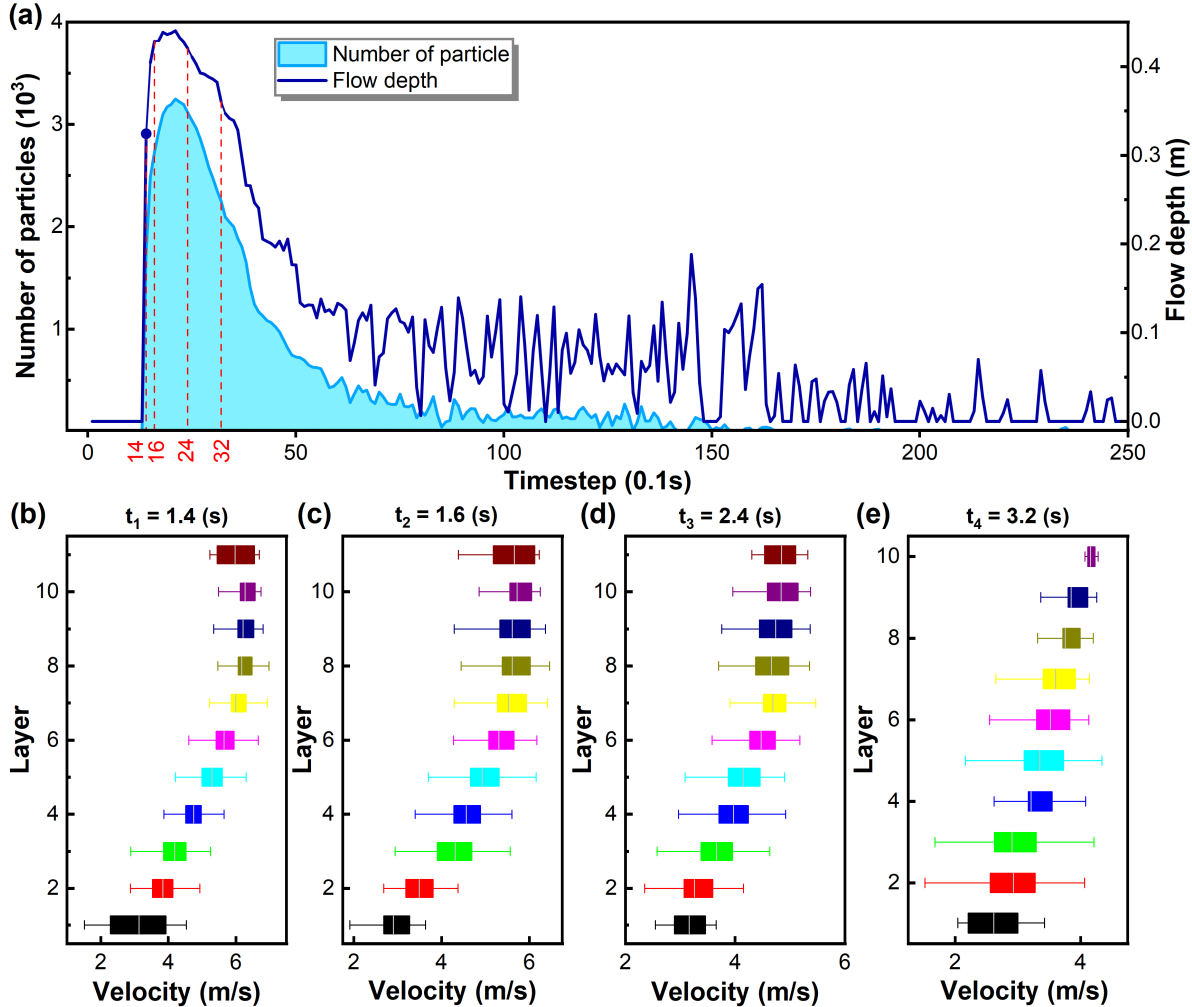
283
 284 **Figure 2.** (a) The USGS flume experiment by Iverson et al. (2011). Reproduced from ref. 26
 285 with permission from the Journal of Geophysical Research Earth Surface, copyright 2012. (b)
 286 The simulation results of flow velocity. (c) Flow front position at different times.

287 3.2 Vertical velocity distribution

288 A cross-section of the flume at the position of $x = 6.0m$ is chosen. We select the cross-section at
 289 this position because behind which a 12cm thick tabular layer of sediment had been covered on
 290 the bottom of the flume in their experiment, within the range of $x = 6.0m$ and $x = 53.0m$.
 291 Combination of basal sliding and internal deformation may arise certainties for exploring
 292 velocity profile.

293 To get a sufficient velocity data, a cross-section domain is generated using $L_{domain} = 0.2m$,
 294 which is 5 times the initial particle distance $dp = 0.04m$. As shown in Figure 2c, a single surge
 295 of debris flow is observed in the numerical simulation result, coincident with the experiment
 296 measurement. Due to that the majority of the debris-flow mass passed through this cross-section

297 during around 1.0s to 5.0s, we choose four different moments, i.e., $t_1 = 1.4s$, $t_2 = 1.6s$,
 298 $t_3 = 2.4s$, and $t_4 = 3.2s$, to explore the temporal variation of the vertical velocity distribution,
 299 as shown in Figure 3. In Figure 3a, the total number of the particles and flow depth belonging to
 300 the selected cross-section is plotted as a function of the simulation time. It is shown that at the
 301 four moments, the total number of the particles are all beyond 2000, providing sufficient data to
 302 investigate the velocity distributions. Normally, we sperate the cross-section into 11 parallel
 303 layers through depth, each of which has around 200 particles with varying velocities v'_X .
 304 Subsequently, the mean velocities \bar{V}_j at different vertical position can be calculated and output
 305 (as shown in Figure 3b-3e).



306

307 **Figure 3.** The result of velocity profile in four time-steps. (a) The total number of the particles
 308 and flow depth over time. (b) The velocity profile at $t_1 = 1.4s$. (c) The velocity profile at
 309 $t_2 = 1.6s$. (d) The velocity profile at $t_3 = 2.4s$. (e) The velocity profile at $t_4 = 3.2s$.

310 It is shown that at all the four moments, the flow velocity presents a nonlinear distribution
 311 through depth. The maximum velocity usually appears at the free surface of the debris flow and
 312 gradually reduces through depth. This phenomenon well matches the possible type of velocity
 313 profile as mentioned in Nagl et al. (2020). As to the temporal variation of debris flow velocity,
 314 the maximum velocity appears at t_1 and t_2 moments, when the front of debris-flow surge arrives

315 and an approximately 6.0m/s velocity is recorded. The velocity is observed gradually decreasing
 316 to around 4.0m/s at the t_4 moment as the majority of debris flow passed, while the division
 317 between the top and bottom velocity seems reduced. It may indicate that debris flow transits into
 318 approximately a constant one after this moment, the phenomenon of which has also been
 319 mentioned in Pudasaini et al. (2020). It should be noticed that at $t_2 = 1.6s$, the velocity at the
 320 free surface ($z = 0.35m \sim 0.40m$) of the main body is slightly smaller, showing a concave-up
 321 profile form developed in the main body as observed in the real-scale experiment in Nagl et al.
 322 (2020). The observed temporal variation of the vertical distribution of the debris-flow velocity
 323 also highlights the necessities to incorporate a time-dependent parameter when regressing the
 324 debris-flow velocity profile.

325 **4 Regression of instantaneous velocity profile**

326 **4.1 Conventional linear velocity profile**

327 As a comparison, we employ the conventional linear law in the previous studies to regress the
 328 velocity profile before we further consider its temporal variation and non-linear features. The
 329 function of linear velocity profile is modified from the original one in Johnson et al. (2012) and
 330 Iverson (2012) and has been used in our previous studies (Han et al., 2018, 2019). The
 331 mathematical expression is

$$V(z) = \bar{V} \left(1 - \alpha + 2\alpha \frac{z}{h} \right) \quad (7)$$

332 where $V(z)$ denotes the velocity profile as velocity at different vertical positions are known. α is
 333 a fitting parameter controlling the amount of shear within the bulk of flow as we mentioned
 334 above. It ranges from $\alpha = 0$ if there is no simple shear to $\alpha = 1$ if there is no basal slip. In
 335 Johnson et al. (2012), a good fit to experimental measurement was suggested with $\alpha = 0.5$. \bar{V} is
 336 the mean velocity of the cross-section at a moment and can be mathematically computed by

$$\bar{V} = \frac{1}{n} \sum_{i=1}^n v'_x(i) \quad (8)$$

337 where n is the total number of the particles belonging to the cross-section domain at a moment.

338 Given this linear velocity profile, the vertical distribution of the velocities in the numerical
 339 results those shown in Figure 3 is regressed. Notice that at each moment, the total number of the
 340 particles and their velocities are varying, resulting in different shapes of velocity profile.
 341 Therefore, we regress the linear velocity profile every 0.08s and obtain different values of the
 342 best fitting parameter α , as shown in Figure 4a. It is obvious that the best fitting values of
 343 parameter α varies from 0.2 to approximately 0.8 during the process, with a mean value of 0.45
 344 which is quite approaching the suggested value by Johnson et al. (2012). Notably, the parameter
 345 α reduces from $\alpha = 0.8$ at the front of debris-flow surge to $\alpha = 0.2$ at the end of surge,
 346 indicating that the main body of the debris flow with internal deformation and shear may evolve
 347 into an approximately constant one with no simple shear.

348 **4.2 Nonlinear velocity profile**

349 The vertical velocity profiles as exhibited in Figure 3 indicate an obvious non-linear velocity
 350 profile, which has been substantiated in the PIV measurements of a flume experiment by Chen et
 351 al. (2017). The nonlinear feature of the velocity profile cannot be well reproduced using the

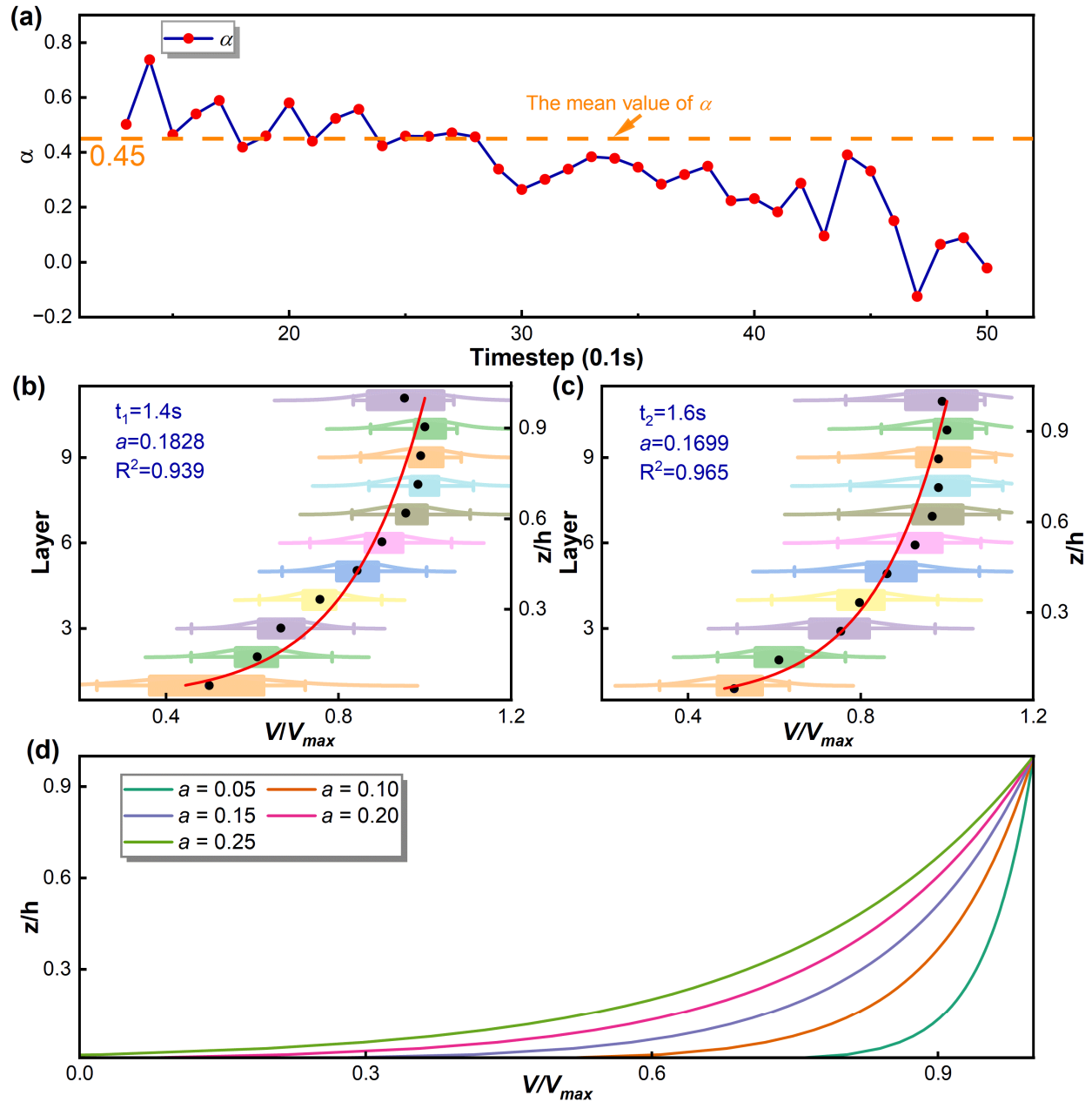
352 above linear velocity profile. In this sense, a nonlinear velocity profile is necessary to illustrate
 353 the complex features of vertical velocity distribution.

354 In this sub-section, regardless of its temporal variation, we choose a logarithmic-based function
 355 to describe the nonlinear velocity profile. To minimize the deviation of debris flow velocity at
 356 different moments, we use dimensionless and normalized terms for the regression, which is

$$\frac{V(z)}{V_{max}} = 1 + a \cdot \ln\left(\frac{z}{h}\right) \quad (9)$$

357 where $V(z)/V_{max}$ is the normalized velocity term ranging in $[0,1]$, denoting the ratios of
 358 velocities at different vertical positions and the maximum velocity V_{max} in the cross-section. z/h
 359 is the normalized vertical position, ranging from $z/h = 0.0$ at the flume bottom to $z/h = 1.0$ at
 360 the free surface of the debris flow. a is an empirical-based fitting parameter controlling the
 361 complex shape of velocity profile.

362 Although sometimes a concave-up profile in the main body has been witnessed, it is still
 363 problematic to obtain a mathematical expression. Therefore, the regressed nonlinear velocity
 364 profile in Eq. (9) ignores concave-up feature and assumes that the maximum velocity appears at
 365 the free surface. To demonstrate the effect, two typical moments at $t_1 = 1.4s$ and $t_2 = 1.6s$ is
 366 used to illustrate the regression, as shown in Figure 4b and 4c. It is shown that two best fitting
 367 values $a = 0.1828$ and $a = 0.1699$ close to each other are obtained, with the satisfactory R-
 368 squared values of $R^2 = 0.939$ and $R^2 = 0.965$. We also explored the influence of parameter a
 369 on the velocity profile, as shown in Figure 4d. It is demonstrated that with an increasing
 370 parameter a , an approximate plug flow ($a < 0.05$) with constant velocity profile evolves into
 371 simple shear flow ($a > 0.25$) with internal deformation.



372

373 **Figure 4.** (a) Temporal variation of the best fitting parameter α of the linear velocity profile. (b)
 374 Velocity profile fitting regression analysis with $t_1 = 1.4s$. (c) Velocity profile fitting regression
 375 analysis with $t_2 = 1.6s$. (d) Analysis of the parameter a of the fitting function.

376 5 Velocity profile considering temporal variation

377 5.1 Mathematical expression

378 As shown in Figure 3, the velocity profiles at four different moments have been witnessed
 379 obvious differences in their shape, indicating that the temporal variation of the debris-flow
 380 velocity profile should be considered. The abovementioned nonlinear profile only considers its
 381 instantaneous shape, therefore, should be improved by incorporating its temporal variation.

382 For this purpose, we introduce a time-linked parameter b in the logarithmic-based velocity
 383 profile in Eq. (10) to describe its temporal variation. The basic form of this temporal-varying,
 384 depth-nonlinear velocity profile is express mathematically as below,

$$\frac{V(z)}{V_{max}} = c + a \cdot \ln\left(\frac{z}{h} + b\right) \quad (10)$$

385 Note that a constraint parameter c is temporally introduced in the above equation, because the
 386 velocity profile should satisfy a basic assumption that maximum velocity V_{max} should appear at
 387 the free surface $z = h$, where the left term of Eq. (10) equates $\frac{V(z)}{V_{max}} = 1.0$. Thus, the constraint
 388 parameter c could be reduced to $c = 1 - a \cdot \ln(1 + b)$. In this way, we obtain a dual-parameter
 389 velocity profile that describes its temporal-varying, depth-nonlinear features,

$$\frac{V(z)}{V_{max}} = 1 + a \cdot \left[\ln\left(\frac{z}{h} + b\right) - \ln(1 + b) \right] \quad (11)$$

390 where a is the fitting parameter controlling the complex shape of velocity profile. b is the time-
 391 linked parameter controlling the temporal variation of the velocity-profile shape.

392 Mathematically, the parameter b poses significant influence to the described velocity profile by
 393 Eq. (11). To explore its influence in detail, a sensitivity analysis on the parameter b is used, we
 394 keep parameter a constant ($a = 0.25$ for simple shear flow is used for instance) but different
 395 values of the parameter b ranging from 0.1 to 0.8 are chosen for sensitivity analysis. The
 396 resulting velocity profiles are shown in the Figure 5a. It demonstrates that the velocity profile
 397 changes gradually from a nonlinear form to a linear one with the increasing value of the
 398 parameter b . It should be noticed that the basal velocity of the debris flow increases from
 399 $0.4V_{max}$ to $0.8V_{max}$ when the parameter b increase from 0.1 to 0.8. It indicates that a greater
 400 value of the parameter b is more adequate for describing the velocity profile of plug flow.

401 5.2 Time-linked parameter b controlling the temporal variation

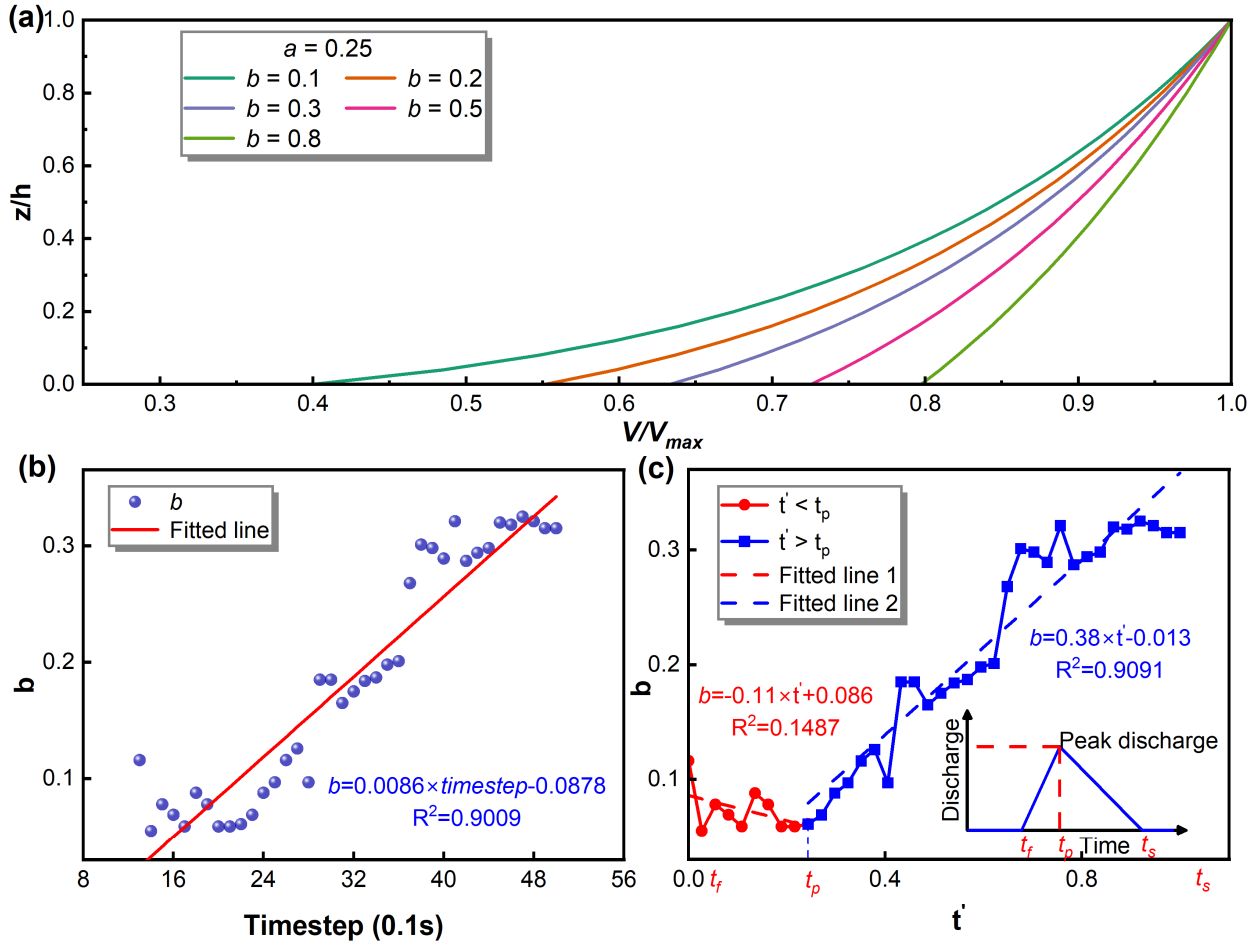
402 As we mentioned above, the parameter b is the time-linked parameter controlling the temporal
 403 variation of the velocity profile shape, therefore, its values should be highly dependent on the
 404 duration of debris-flow process. In this section, we attempt to explore the link between the value
 405 of the parameter b and the time t , which is supposed as a mathematical function of $b = f(t)$.

406 In Section 3, we estimated and documented the velocities at different vertical locations and at
 407 different moments in the USGS flume experiment using the proposed 3D-HBP-SPH model.
 408 These time-series data provide supports for investigation the details of $b = f(t)$. Because the
 409 majority of debris-flow mass passed through the chosen cross-section at $x = 6.0m$ within 5
 410 seconds since debris flow released, we separate the duration between 1~5 second into 50
 411 timesteps, with a time increment of 0.1s. A constant value $a = 0.25$ is used in each timestep,
 412 while the best fitting value of the parameter b is obtained. Subsequently, the best fitting values of
 413 the parameter b in time-series are plotted as a function of time t , as shown in Figure 5b. It is
 414 obvious that the parameter b gradually increases from $b = 0.05$ to $b = 0.30$ with the debris-flow
 415 duration. We use a linear function to regress the relation between b and t . The obtained linear
 416 function shows a satisfactory R-squared value (>0.90), demonstrating a strong linear relation
 417 between b and t .

418 However, it should be mentioned that the direct usage of the regressed linear function between b
 419 and t is limited, because debris-flow duration t significantly varies case by case, even multiple
 420 surges are often observed in a single debris-flow event. In this sense, debris-flow duration t is
 421 not adequate for directly evaluating the parameter b . Here, we introduce a concept of the
 422 normalized time t' in an individual surge to address this issue. For the multi-surge debris flow,
 423 each individual surge is separated and then is assumed to follow the triangular hydrograph
 424 (Takaoka et al., 2006) as shown in Figure 5c. The single-surge hydrograph has a rising limb,
 425 falling limb, and tail limb, wherein three major moments are required to reproduce this
 426 hydrograph; t_f represents the moment when debris-flow front arrives the cross-section, t_p
 427 represents the debris-flow peak, and t_s represents the moment when debris-flow surge ends.
 428 Using this hydrograph, the proposed normalized time t' in an individual surge is expressed as

$$t' = \frac{t - t_f}{t_s - t_f}, t \in [t_f, t_s] \quad (12)$$

429 In Eq. (12), the term of $t_s - t_f$ denotes the duration of the individual debris-flow surge.



430

431 **Figure 5.** (a) Velocity profile corresponding to different parameter b . (b) The relationship
 432 between parameter b and time. (c) The relationship between parameter b and relative time t' .

433 In this way, the time-series data of the best fitting values for the parameter b can be represented
 434 as a function of the normalized time t' , as shown in [Figure 5c](#). In accordance with the triangular
 435 hydrograph we assumed, the variation of the parameter b shows two obvious stages divided by
 436 the peak moment ($t' = 0.21$), as marked in red and blue line in [Figure 5c](#). The red line denotes
 437 the time-to-peak stage ($t' \in [0, 0.21]$), when the best fitting value of the parameter b decreases
 438 with t' . While the blue line demonstrates the time-after-peak stage ($t' \in [0.21, 1.00]$), in
 439 contrast, the best fitting value of the parameter b gradually increases with t' . As indicated in
 440 [Figure 5c](#), linear relation between b and t' at both stages are observed, which are regressed as

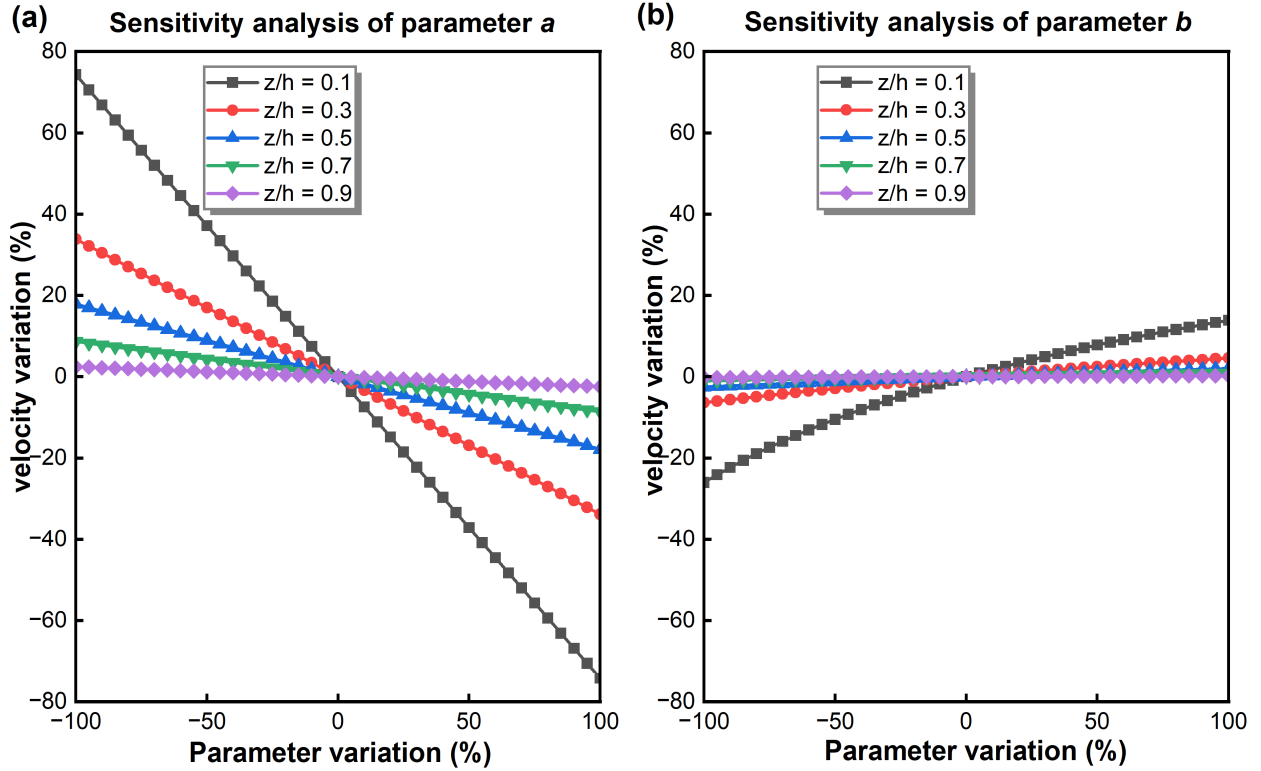
$$b = \begin{cases} -0.11t' + 0.086, & t' < t_p \\ 0.38t' - 0.013, & t' \geq t_p \end{cases} \quad (13)$$

441 **6 Discussion**

442 As demonstrated in [Section 4.2](#), the proposed velocity profile contains two crucial parameters a
 443 and b , which are used to describe the nonlinear characteristics and temporal evolution
 444 characteristics of the vertical velocity distribution of debris flow, respectively. In order to better
 445 understand the proposed model, we discuss the model sensitivities and verify the model in this
 446 section.

447 **6.1 Sensitivity analysis of the parameter a and b**

448 A one-at-a-time sensitivity analysis is performed to assess the impact of input parameters'
 449 variation on the improved nonlinear model. All the initial parameters are kept constant except the
 450 one chosen for sensitivity analysis. [Figure 6](#) shows the velocity of debris flow as a function of
 451 the chosen parameters a and b . As shown in [Figure 6](#), the velocity through the depth decreases
 452 with the increase of parameter a but increases as a function of the parameter b . It is indicated
 453 that the parameter a shows a more obvious impact compared to b because velocities approaching
 454 the bottom ($\frac{z}{h} = 0.1$) vary approximately $\pm 80\%$ when the value of a varies $\pm 100\%$, it is almost
 455 3.5 times greater compared to the impact of the parameter b . [Figure 6](#) also demonstrates that both
 456 two parameters pose more significant influence on the velocities approaching the bottom than the
 457 free surface.



458

459 **Figure 6.** Variation of the resulting in velocities at different vertical location as a function of the
 460 parameter a and b . (a) Sensitivity analysis of the parameter a . (b) Sensitivity analysis of the
 461 parameter b .

462 6.2 Verification using velocity measurement data in previous experiments

463 In order to verify the proposed velocity profile, we use 34 sets of the measured velocity data
 464 from three individual flume experiments as reported by Egashira et al. (1989), Hotta et al.
 465 (1998), and Chen et al. (2017). The velocity profiles of these experiments are regressed using the
 466 proposed model and compared with the existing linear model.

467 Owing to that the velocity measurement data in three experiments were the mean velocities at the
 468 stage approaching to peak, and the details of their temporal variation are not available.

469 Therefore, in this section, a constant mean value of the time-link parameter $b = 0.10$ is pre-
 470 defined, owing to that the parameter b ranges from 0.05 to 0.15 at the stage approaching to peak
 471 as shown in Figure 5c. In order to evaluate the fitting performance of the proposed model, the
 472 residual sum of squares (RSS) is used, which is

$$RSS = \sum_{i=1}^n (l_i - v_i)^2 \quad (14)$$

473 where l_i represents the measured velocity value, v_i represents the velocity estimated by the
 474 proposed non-linear profile, and n denotes the number of measured data points in each set of the
 475 flume experiment. A smaller value of RSS indicate a better fitting effect.

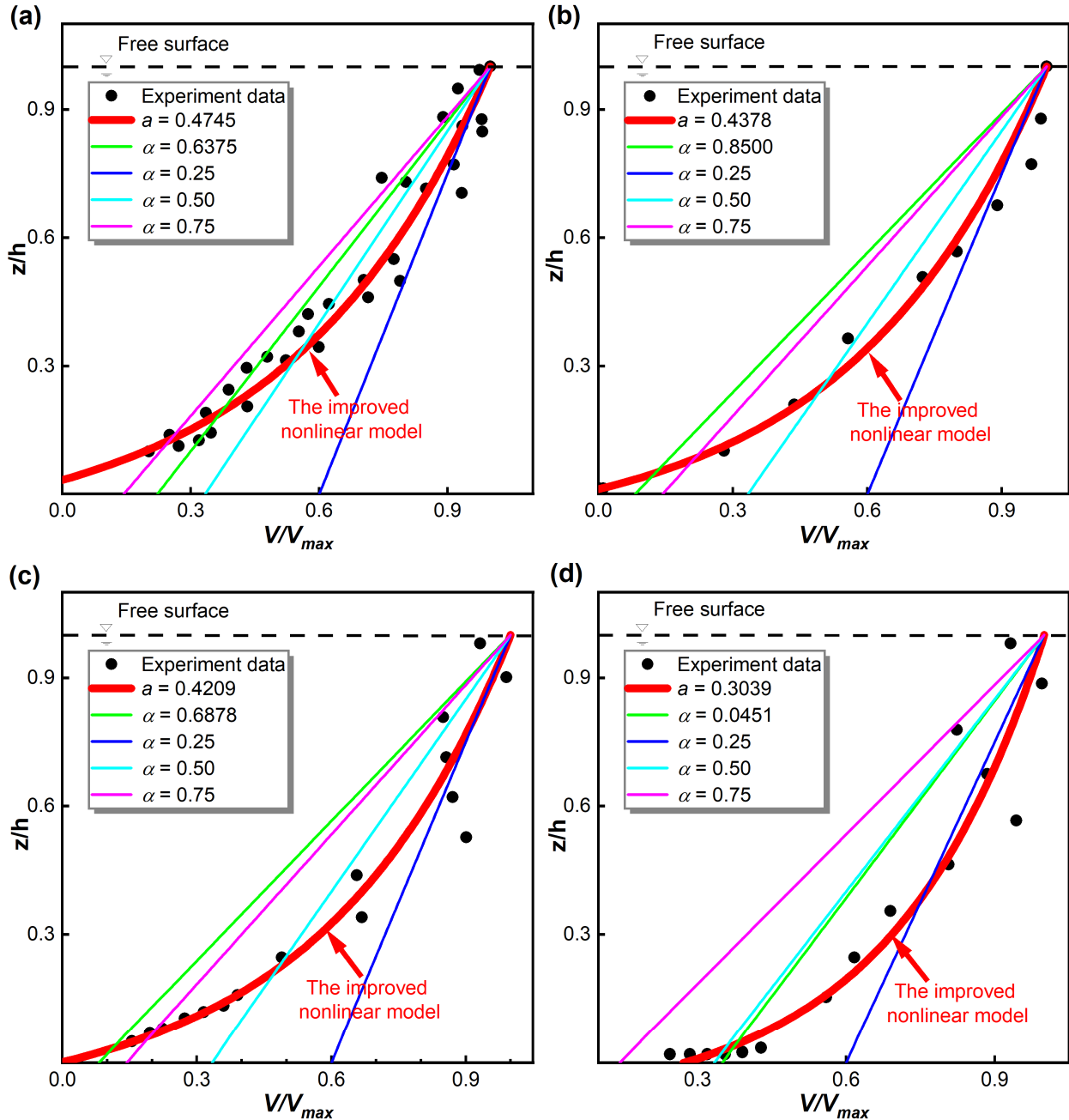
476 Results are listed in detail in Table 1, in which Data 1-8 use the flume experiment data by
 477 Egashira et al. (1989), Data 9-10 by Hotta et al. (1998), while the remaining by Chen et al.
 478 (2017). As a comparison, the previous linear velocity profile as introduced in Eq. (7) is used for

479 comparison, with the suggested values of the fitting parameter α , i.e., $\alpha = 0.25$, $\alpha = 0.50$, and
 480 $\alpha = 0.75$, are used respectively (Iverson, 2012; Johnson et al., 2012). It is obvious that the
 481 proposed non-linear velocity profile attains better fitting results for 32 sets among all the 34 sets
 482 of experiments (The summary of fitting results for 34 sets of experimental data is included in the
 483 supporting information Figures S1 to S34, among which 4 groups of data are shown in Figure 7).
 484 Results indicate that the proposed velocity profile is more consistent with the experimental data
 485 when describing the debris flow velocity.

486 **Table 1.** Fitting results of experimental data from Egashira et al. (1989), Hotta et al. (1998) and
 487 Chen et al. (2017).

Data id	The proposed non-linear velocity profile		The previous linear velocity profile				
	a	$RSS(a)$	α	$RSS(\alpha)$	$RSS(\alpha = 0.25)$	$RSS(\alpha = 0.50)$	$RSS(\alpha = 0.75)$
1	0.3897	0.0713	0.4767	0.2838	0.0216	0.0079	0.0248
2	0.4651	0.2368	0.5270	0.2530	0.0479	0.0102	0.0103
3	0.4745	0.0863	0.6375	0.3295	0.0433	0.0073	0.0096
4	0.5148	0.3158	0.6315	0.5065	0.0566	0.0100	0.0056
5	0.2787	0.1097	0.3046	0.2335	0.0079	0.0184	0.0516
6	0.4529	0.6525	0.3844	0.5122	0.0506	0.0174	0.0193
7	0.3869	0.2844	0.3498	0.2299	0.0210	0.0064	0.0208
8	0.4102	0.1055	0.5022	0.3186	0.0215	0.0070	0.0226
9	0.4378	0.0134	0.8500	0.3052	0.0870	0.0257	0.0166
10	0.4639	0.0350	0.7144	0.2753	0.0762	0.0214	0.0114
11	0.3402	0.0750	0.4902	0.7263	0.0329	0.0170	0.0472
12	0.4452	0.0534	0.8574	3.4257	0.1412	0.0391	0.0132
13	0.3624	0.1053	0.5792	1.0299	0.0547	0.0231	0.0423
14	0.4041	0.3445	0.5418	2.2549	0.0826	0.0356	0.0444
15	0.5288	0.2206	1.1107	2.1595	0.1821	0.0583	0.0132
16	0.3332	0.0590	0.5198	0.7172	0.0391	0.0160	0.0423
17	0.2902	0.0631	0.3680	0.4148	0.0148	0.0174	0.0620
18	0.3730	0.1994	0.7136	2.3323	0.0977	0.0299	0.0301
19	0.4209	0.0373	0.6878	0.8234	0.0681	0.0139	0.0157
20	0.3096	0.0424	0.4275	0.4702	0.0216	0.0103	0.0462
21	0.3437	0.4079	0.4859	2.5437	0.0793	0.0239	0.0358
22	0.3599	0.4702	0.6016	3.9330	0.1131	0.0393	0.0382
23	0.2697	0.0850	0.3281	0.7398	0.0225	0.0268	0.0831
24	0.3445	0.2249	0.5693	2.7017	0.0823	0.0283	0.0428
25	0.3285	0.1180	0.5183	1.0082	0.0461	0.0259	0.0547
26	0.2990	0.1988	0.3739	1.3356	0.0449	0.0296	0.0707
27	0.3872	0.0514	0.6067	3.4303	0.1571	0.0436	0.0082
28	0.3315	0.1120	0.5828	2.3820	0.0708	0.0238	0.0433
29	0.2667	0.0805	0.3140	0.7858	0.0211	0.0256	0.0827

30	0.3649	0.1024	0.5753	0.7953	0.0623	0.0373	0.0554
31	0.2849	0.1200	0.4387	1.2753	0.0439	0.0297	0.0742
32	0.3282	0.2810	0.4569	1.7309	0.0576	0.0334	0.0623
33	0.4143	0.0632	0.8013	4.6371	0.1523	0.0429	0.0177
34	0.3039	0.0451	0.4820	0.6970	0.0354	0.0103	0.0394



488

489 **Figure 7.** Comparison of the improved nonlinear distribution model and the linear model. (a)

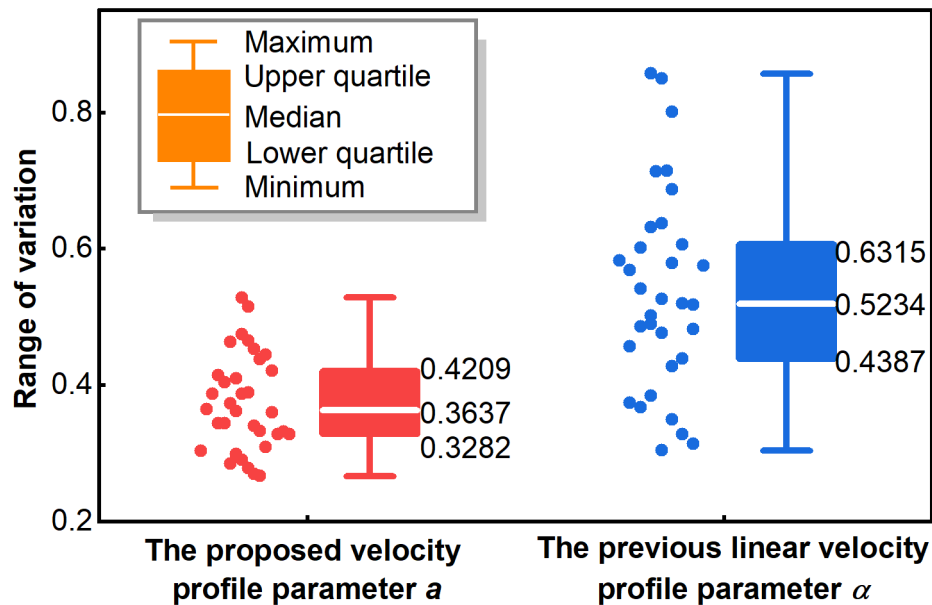
490 Experiment data 3. (b) Experiment data 9. (c) Experiment data 19. (d) Experiment data 34.

491

492 6.3 Suggestion for the rational value of the parameters

493 Sensitivities of the key parameters in proposed profile has been discussed in section 6.1, while in
 494 this section, the suggested value and the rational range of the key parameters are discussed,
 495 which will be beneficial for practical work. Ideally, a great value range of the parameter may
 496 somewhat arise difficulties for practical work if no criteria is provided. This issue has long been
 497 highlighted, such as the viscosity coefficient in debris-flow rheology, the rational value of which
 498 may vary from a few tens to hundreds of times from measurement (Takahashi, 2009; Han et al.,
 499 2017). As to the time-linked parameter b , the expected value could be calculated by Eq. (13)
 500 under the assumption of triangular hydrograph. For the cases those excluding the consideration
 501 of temporal variation, a rational range of $b \in [0.05, 0.15]$ as shown in Figure 5c could be
 502 referred to, with a suggested value of $b = 0.10$ for estimating the mean velocity around the peak.

503 In contrast, it is more complex to discuss the rational range of the parameter a because this
 504 parameter is empirical based. In this section, we provide the suggestion for the rational value of
 505 the parameter a based on the above-mentioned verification using 34 sets of experiments. As
 506 shown in Figure 8, the median of the best fitting value of the parameter a for all 34 sets of the
 507 experiments is 0.3637, while the maximum and the minimum value are 0.5288 and 0.2667,
 508 respectively. Figure 8 also demonstrates that half of the best fitting values of the parameter a fall
 509 within the range of $[0.3282, 0.4209]$, which is smaller and better comparing to the parameter
 510 $\alpha \in [0.4387, 0.6315]$ in conventional linear velocity profile. As such, a rational range of
 511 $a \in [0.32, 0.42]$ could be referred to, with a suggested value of $a = 0.36$ for a benchmark for
 512 calibration.



513
 514 **Figure 8.** Suggestion and comparison for the rational range of the empirical parameter a and α
 515 in the proposed and previous velocity profiles, respectively.

516 7 Discussion

517 In this paper, we propose a new approach to explore the temporal-varying and depth-nonlinear
 518 velocity profile of debris flows. The debris-flow process is simulated by our previous 3D-HBP-
 519 SPH numerical model and recorded in time-series data in particle form. To interpret and analyse

520 the details of debris-flow dynamics, a stratification statistical algorithm that suitable for SPH
521 particles is proposed, upon which the temporal velocities of debris flow at different mud depths
522 during the process could be obtained.

523 The flume experiments by USGS in the previous study is simulated in order to explore the
524 debris-flow velocity profile. A logarithmic-based nonlinear function is proposed for reproducing
525 the debris-flow velocity profile in detail. The proposed function contains two key parameters, the
526 empirical parameter a controlling the shape of velocity profile, and the time-linked parameter b
527 concerning its temporal evolution. A function connecting the parameter b to the normalized time
528 t' is regressed in particular for the debris flows with the assumed triangular hydrograph.

529 We verify the proposed velocity profile and explore its sensitivity using 34 sets of velocity data
530 from the three individual flume experiments in previous literatures. Results indicate the rational
531 range of the values for both parameters, wherein $a \in [0.32, 0.42]$ and $b \in [0.05, 0.15]$ are
532 suggested. The conventional linear velocity profiles summarized in previous studies are used for
533 comparison. It is shown that the proposed depth-nonlinear and temporal-varying velocity profile
534 performs better than previous ones.

535 **Acknowledgments**

536 This study was financially supported by the National Natural Science Foundation of China
537 (Grant No. 52078493); the Natural Science Foundation of Hunan Province (Grant No.
538 2022JJ30700); the Natural Science Foundation for Excellent Young Scholars of Hunan (Grant
539 No. 2021JJ20057); the Innovation Provincial Program of Hunan Province (Grant No.
540 2020RC3002). These financial supports are gratefully acknowledged.

541 **Author contributions**

542 Z.H. directed the program. W.D.X. and C.C.Z performed all the simulations. Z.H., W.D.X and
543 Y.G.L. wrote the manuscript with the help and advice from W.D.W. and G.Q.C. N.S.C. and
544 G.S.H. reviewed and edited the manuscript. All authors participated in data analysis, discussed
545 the results and co-edited the manuscript. All authors participated in data analysis, discussed the
546 results and co-edited the manuscript.

547 **Competing interests**

548 The authors declare no competing interests.

549 **Data Availability Statement**

550 The detailed information of the USGS flume experiment simulated in this study can be obtained
551 at <https://doi.org/10.1038/ngeo1040>. The SPH implementation code used in this study can be
552 obtained at <https://github.com/DualSPHysics>. The modeling parameters of this study can be
553 obtained at <https://doi.org/10.3390/W14091352>. The experimental data used to validate the
554 proposed model in this study can be obtained at [https://github.com/dreamer0501/The-validation-](https://github.com/dreamer0501/The-validation-data)
555 [data](https://github.com/dreamer0501/The-validation-data).

556 **References**

557 Arai, M., Huebl, J., & Kaitna, R. (2013), Occurrence conditions of roll waves for three grain-
558 fluid models and comparison with results from experiments and field observation.

- 559 *Geophysical Journal International*, 195(3), 1464-1480.
 560 <https://doi.org/10.1093/gji/ggt352>
- 561 Arattano, M., & Marchi, L. (2005), Measurements of debris flow velocity through cross-
 562 correlation of instrumentation data. *Natural Hazards and Earth System Science*, 5(1),
 563 137-142. <https://doi.org/10.5194/nhess-5-137-2005>
- 564 Chen, H., Hu, K., Cui, P., & Chen, X. (2017), Investigation of vertical velocity distribution in
 565 debris flows by PIV measurement. *Geomatics, Natural Hazards and Risk*, 8(2), 1631-
 566 1642. <https://doi.org/10.1080/19475705.2017.1366955>
- 567 Chen, H.X., Li, J., Feng, S.J., Gao, H.Y., & Zhang, D.M. (2019), Simulation of interactions
 568 between debris flow and check dams on three-dimensional terrain. *Engineering Geology*,
 569 251, 48-62. <https://doi.org/10.1016/j.enggeo.2019.02.001>
- 570 Dowling, C.A., & Santi, P.M. (2014), Debris flows and their toll on human life: A global
 571 analysis of debris-flow fatalities from 1950 to 2011. *Natural Hazards*, 71(1), 203-227.
 572 <https://doi.org/10.1007/S11069-013-0907-4>
- 573 Du, C., Wu, W.M., & Ma, C. (2021), Velocity profile of debris flow based on quadratic rheology
 574 model. *Journal of Mountain Science*, 18(8), 2120-2129. <https://doi.org/10.1007/s11629-021-6790-7>
- 575
- 576 Egashira, S., Ashida, K., Yajima, H., & Takahama, J. (1989), Constitutive equation of debris
 577 flow. *Annuals Disaster Prevention Research Institute, Kyoto University*, 32(2), 487-501.
- 578 Gabriele, A., Tsoligkas, A.N., Kings, I.N., & Simmons, M.J.H. (2011), Use of PIV to measure
 579 turbulence modulation in a high throughput stirred vessel with the addition of high Stokes
 580 number particles for both up- and down-pumping configurations. *Chemical Engineering*
 581 *Science*, 66(23), 5862-5874. <https://doi.org/10.1016/j.ces.2011.08.007>
- 582 Godt, J.W. & Coe, J.A. (2007), Alpine debris flows triggered by a 28 July 1999 thunderstorm in
 583 the central Front Range, Colorado. *Geomorphology*, 84(1-2), 80-97.
 584 <https://doi.org/10.1016/j.geomorph.2006.07.009>
- 585 Han, Z., Chen, G., Li, Y., Wang, W., & Zhang, H. (2015a), Exploring the velocity distribution of
 586 debris flows: An iteration algorithm based approach for complex cross-sections.
 587 *Geomorphology*, 241, 72-82. <https://doi.org/10.1016/j.geomorph.2015.03.043>
- 588 Han, Z., Chen, G., Li, Y., Tang, C., Xu, L., He, Y., Huang, X., & Wang, W. (2015b), Numerical
 589 simulation of debris-flow behavior incorporating a dynamic method for estimating the
 590 entrainment. *Engineering Geology*, 190, 52-64.
 591 <https://doi.org/10.1016/j.enggeo.2015.02.009>
- 592 Han, Z., Chen, G., Li, Y., & He, Y. (2015c), Assessing entrainment of bed material in a debris-
 593 flow event: A theoretical approach incorporating Monte Carlo method. *Earth Surface*
 594 *Processes and Landforms*, 40(14), 1877-1890. <https://doi.org/10.1002/esp.3766>
- 595 Han, Z., Chen, G., Li, Y., Xu, L., Zheng, L., & Zhang, Y. (2014), A new approach for analyzing
 596 the velocity distribution of debris flows at typical cross-sections. *Natural Hazards*, 74(3),
 597 2053-2070. <https://doi.org/10.1007/S11069-014-1276-3/FIGURES/14>
- 598 Han, Z., Li, Y.G., Huang, J.L., Chen, G.Q., Xu, L.R., Tang, C., Zhang, H., & Shang, Y.H.
 599 (2017), Numerical simulation for run-out extent of debris flows using an improved
 600 cellular automaton model. *Bulletin of Engineering Geology and The Environment*, 76(3),
 601 961-974. <https://doi.org/10.1007/s10064-016-0902-6>
- 602 Han, Z., Su, B., Li, Y., Wang, Wei, Wang, Weidong, Huang, J., & Chen, G. (2019), Numerical
 603 simulation of debris-flow behavior based on the SPH method incorporating the Herschel-

- 604 Bulkley-Papanastasiou rheology model. *Engineering Geology*, 255, 26-36.
 605 <https://doi.org/10.1016/j.enggeo.2019.04.013>
- 606 Han, Z., Wang, W., Li, Y., Huang, J., Su, B., Tang, C., Chen, G., & Qu, X. (2018), An integrated
 607 method for rapid estimation of the valley incision by debris flows. *Engineering Geology*,
 608 232, 34-45. <https://doi.org/10.1016/j.enggeo.2017.11.007>
- 609 Han, Z., Yang, F., Li, Y., Dou, J., Chen, N., Hu, G., Chen, G., & Xu, L. (2021a), GIS-Based
 610 Three-Dimensional SPH Simulation for the 11 April 2018 Yabakei Landslide at Oita
 611 Nakatsu, Japan. *Water*, 13(21), 3012. <https://doi.org/10.3390/W13213012>
- 612 Han, Z., Zeng, C., & Li, Y. (2021b), Nonlinear vertical velocity distribution of debris flows
 613 using fluid-particle hierarchical statistical algorithm (in Chinese). *Journal of Engineering*
 614 *Geology*, 1-12. <https://doi.org/10.13544/j.cnki.jeg.2021-0545>
- 615 Han, Z., Zeng, C., & Li, Y. (2022), Hierarchical statistics-based nonlinear vertical velocity
 616 distribution of debris flow and its application in entrainment estimation. *Water*, 14(9),
 617 1352. <https://doi.org/10.3390/W14091352>
- 618 Hotta, N., Miyamoto, K., Suzuki, M., & Ohta, T. (1998), Pore-water pressure distribution of
 619 solid-water phase flow in a rolling mill. *Journal of the Japan Society of Erosion Control*
 620 *Engineering*, 50(6), 11-16. <https://doi.org/10.11475/sabo1973.50.6.11>
- 621 Hotta, N., & Ohta, T. (2000), Pore-Water pressure of debris flows. *Physics and Chemistry of the*
 622 *Earth, Part B: Hydrology, Oceans and Atmosphere*, 25(4), 381-385.
 623 [https://doi.org/10.1016/S1464-1909\(00\)00030-7](https://doi.org/10.1016/S1464-1909(00)00030-7)
- 624 Huang, G., Lv, G., Zhang, S., Huang, D., Zhao, L., Ni, X., Liu, H., Lv, J., & Liu, C. (2022).
 625 Numerical analysis of debris flows along the Sichuan-Tibet railway based on an
 626 improved 3D sphere DDA model and UAV-based photogrammetry. *Engineering*
 627 *Geology*, 305, 106722. <https://doi.org/10.1016/J.ENGGEOL.2022.106722>
- 628 Hungr, O., & McDougall, S. (2009). Two numerical models for landslide dynamic analysis.
 629 *Computers and Geosciences*, 35(5), 978-992.
 630 <https://doi.org/10.1016/j.cageo.2007.12.003>
- 631 Iverson, R.M. (2012). Elementary theory of bed-sediment entrainment by debris flows and
 632 avalanches. *Journal of Geophysical Research: Earth Surface*, 117(3), F03006.
 633 <https://doi.org/10.1029/2011JF002189>
- 634 Iverson, R.M. (1997). The physics of debris flows. *Reviews of Geophysics*, 35(3), 245–296.
 635 <https://doi.org/10.1029/97RG00426>
- 636 Iverson, R.M., Reid, M.E., Logan, M., LaHusen, R.G., Godt, J.W., & Griswold, J.P. (2011).
 637 Positive feedback and momentum growth during debris-flow entrainment of wet bed
 638 sediment. *Nature Geoscience*, 4(2), 116-121. <https://doi.org/10.1038/ngeo1040>
- 639 Iverson, R.M., & Vallance, J.W. (2001). New views of granular mass flows. *Geology*, 29(2),
 640 115-118. [https://doi.org/10.1130/0091-7613\(2001\)029<0115:NVOGMF>2.0.CO;2](https://doi.org/10.1130/0091-7613(2001)029<0115:NVOGMF>2.0.CO;2)
- 641 Johnson, C.G., Kokelaar, B.P., Iverson, R.M., Logan, M., Lahusen, R.G., & Gray, J.M.N.T.
 642 (2012). Grain-size segregation and levee formation in geophysical mass flows. *Journal of*
 643 *Geophysical Research: Earth Surface*, 117(1), F01032.
 644 <https://doi.org/10.1029/2011JF002185>
- 645 Liu, P., & Lam, K.M. (2015). Simultaneous PIV measurements of fluid and particle velocity
 646 fields of a sediment-laden buoyant jet. *Journal of Hydro-Environment Research*, 9(2),
 647 314-323. <https://doi.org/10.1016/j.jher.2014.07.007>

- 648 Luna, B. Q., Remaître, A., van Asch, T. W. J., Malet, J. P., & van Westen, C. J. (2012). Analysis
 649 of debris flow behavior with a one dimensional run-out model incorporating entrainment.
 650 *Engineering Geology*, 128, 63-75. <https://doi.org/10.1016/j.enggeo.2011.04.007>
- 651 McDougall, S., & Hungr, O. (2005). Dynamic modelling of entrainment in rapid landslides.
 652 *Canadian Geotechnical Journal*, 42(5), 1437-1448. <https://doi.org/10.1139/t05-064>
- 653 Morikawa, D.S., & Asai, M. (2022). A phase-change approach to landslide simulations:
 654 Coupling finite strain elastoplastic TLSPH with non-Newtonian IISPH. *Computers and*
 655 *Geotechnics*, 148, 104815. <https://doi.org/10.1016/J.COMPGEO.2022.104815>
- 656 Nagl, G., Hübl, J., & Kaitna, R. (2020). Velocity profiles and basal stresses in natural debris
 657 flows. *Earth Surface Processes and Landforms*, 45(8), 1764-
 658 <https://doi.org/10.1002/esp.4844>
- 659 Ouyang, C., He, S., & Tang, C. (2015). Numerical analysis of dynamics of debris flow over
 660 erodible beds in Wenchuan earthquake-induced area. *Engineering Geology*, 194, 62-72.
 661 <https://doi.org/10.1016/j.enggeo.2014.07.012>
- 662 Prochaska, A.B., Santi, P.M., Higgins, J.D., & Cannon, S.H. (2008). A study of methods to
 663 estimate debris flow velocity. *Landslides*, 5(4), 431-444. [https://doi.org/10.1007/s10346-](https://doi.org/10.1007/s10346-008-0137-0)
 664 [008-0137-0](https://doi.org/10.1007/s10346-008-0137-0)
- 665 Pudasaini, S.P., & Fischer, J.T. (2020). A mechanical erosion model for two-phase mass flows.
 666 *International Journal of Multiphase Flow*, 132, 103416.
 667 <https://doi.org/10.1016/j.ijmultiphaseflow.2020.103416>
- 668 Remaître, A., W. J. Van Asch, T., Malet, J.P., & Maquaire, O. (2008). Influence of check dams
 669 on debris-flow run-out intensity. *Natural Hazards and Earth System Science*, 8(6), 1403-
 670 1416. <https://doi.org/10.5194/nhess-8-1403-2008>
- 671 Rickenmann, D. (1999). Empirical relationships for debris flows. *Natural Hazards*, 19(1), 47-77.
 672 <https://doi.org/10.1023/A:1008064220727>
- 673 Takaoka, H., Hashimoto, H., Ikematsu, S., & Hikida, M. (2006). Prediction of landslide-induced
 674 debris flow hydrograph: The Atsumari debris flow disaster in Japan. *WIT Transactions*
 675 *on Ecology and the Environment*, 90, 27-36. <https://doi.org/10.2495/DEB060031>
- 676 Takahashi, T. (2009). A review of Japanese debris flow research. *International journal of*
 677 *erosion control engineering*, 2(1), 1–14.
- 678 Tang, C., Rengers, N., van Asch, T.W.J., Yang, Y.H., & Wang, G.F. (2011). Triggering
 679 conditions and depositional characteristics of a disastrous debris flow event in Zhouqu
 680 city, Gansu Province, northwestern China. *Natural Hazards and Earth System Science*,
 681 11(11), 2903-2912. <https://doi.org/10.5194/nhess-11-2903-2011>
- 682 Tecca, P.R., Deganutti, A.M., Genevois, R., & Galgaro, A. (2003). Velocity distributions in a
 683 coarse debris flow. In: Chen, R. (Ed.), *Debris-Flow Hazards Mitigation: Mechanics,*
 684 *Prediction, and Assessment Proceedings*. Millpress, Rotterdam, The Netherlands (pp,
 685 905–916).
- 686 VanDine, D.F., & Bovis, M. (2002). History and goals of Canadian debris flow research, a
 687 review. *Natural Hazards*, 26(1), 69-82.
- 688 Wei, F., & Hu, K. (2009). Review and trends on debris flow velocity research (in Chinese).
 689 *Journal of Mountain Science*, 27(5), 545–550.
- 690 Wei, F., Yang, H., Hu, K., & Chernomorets, S. (2012). Measuring internal velocity of debris
 691 flows by temporally correlated shear forces. *Journal of Earth Science*, 23(3), 373-380.
 692 <https://doi.org/10.1007/s12583-012-0258-1>

- 693 Yu, D., Tang, L., & Chen, C. (2020). Three-dimensional numerical simulation of mud flow from
694 a tailing dam failure across complex terrain. *Natural Hazards and Earth System Sciences*,
695 20(3), 727-741. <https://doi.org/10.5194/nhess-20-727-2020>
- 696 Zanuttigh, B., & Lamberti, A. (2007). Instability and surge development in debris flows. *Reviews*
697 *of Geophysics*, 45(3), RG3006. <https://doi.org/10.1029/2005RG000175>